CHEMISTRY OF MATERIALS

ARTICLE

pubs.acs.org/cm

Hydrothermal Treatment of a Hematite Film Leads to Highly Oriented Faceted Nanostructures with Enhanced Photocurrents

Debajeet K. Bora,*[,†,‡] Artur Braun,[†] Rolf Erni,[§] Giuseppino Fortunato,[∥] Thomas Graule,[†,¶] and Edwin C. Constable[‡]

[†]Laboratory for High Performance Ceramics, Empa. Swiss Federal Laboratories for Materials Science and Technology, CH-8600 Dübendorf, Switzerland

[‡]Department of Chemistry, University of Basel, CH-4056 Basel, Switzerland

[§]Electron Microscopy Center, Empa. Swiss Federal Laboratories for Materials Science and Technology, CH-8600 Dübendorf, Switzerland

[∥]Laboratory for Advanced Fibers, Empa. Swiss Federal Laboratories for Materials Science and Technology, CH-9014 St. Gallen, Switzerland

[¶]Technische Universität Bergakademie Freiberg, D-09596 Freiberg, Germany

Supporting Information

ABSTRACT: A simple one-pot hydrothermal method is described for converting a dip-coated hematite nanoparticulate film into an array of nanorods with superimposed flowerlike structures suitable for water splitting in photoelectrochemical cells. The hydrothermal treatment of the dip-coated hematite film with $FeCl_3 \cdot 6H_2O$ and L-arginine enhances the photocurrent by a factor of 2. It has been found that hydrothermal treatment changes the optical properties of the pristine hematite film, but the energy band gap (E_g) does not change significantly to show some electronic effect. X-ray diffractograms of pristine and hydrothermally modified films reveal evolution of preferential orientations and textures. Electron micrographs show that the particles are more prismatic after modification, with a size of around 40 nm × 200 nm. The X-ray photoelectron spectroscopy valence-band spectra point at a depletion of the spectral intensity near the Fermi energy upon hydrothermal modification. The photocurrent density of the pristine film reached 218 μA/cm^2 after 48 h of hydrothermal treatment, and this increase was found to be due to the higher specific surface area of the modified film and changes in the optical properties of the pristine film after hydrothermal treatment.

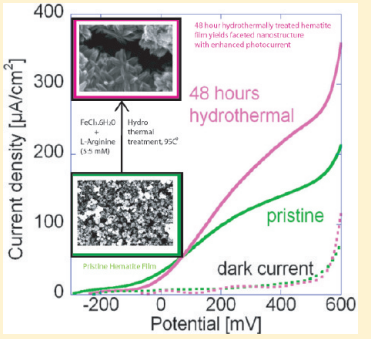

KEYWORDS: hematite thin film, photocurrent, hydrothermal treatment, faceted nanostructures, flowerlike superstructures

INTRODUCTION

Hematite thin films are interesting for photochemical water oxidation[1−5] because of their stability, suitable band gap, and energy band positions, but their reported efficiencies are relatively low. Optimization of their photocurrent densities has been achieved either through doping[6] or by morphological modification. Doping with silicon resulted in the formation of dendritic nanostructures and a significant increase in the incident photon-to-current conversion efficiency of 42% at 320 nm wavelength.[7] The suggested physical rationale for the increased photocurrent is minimization of the distance that the photogenerated electron holes have to overcome to arrive at the semiconductor−liquid interface. Hierarchical nanoarchitectures can also increase the efficiency.[8] The efficiency and photocorrosion stability of photoelectrode materials are also linked to the surface chemistry of crystal facets.[9] In hematite, the surface structure and chemistry of the (001) surface play an important role in the catalytic activity and electronic conductivity.[10] In niobium-doped single-crystal platelets of hematite, the (001) basal plane exposed to the electrolyte exhibits a good efficiency in water oxidation.[11] While substitution and doping can lead to an improved electronic structure and thus enhanced functionality, the influence of the morphology on the performance of the materials should not be underestimated.

The development of different hematite-based hierarchical nanoarchitectures such as nanowires, nanobelts, nanotubes, nanorods, flowerlike, urchinlike, and elliptic superstructures, or dendritic micropines is an emerging strategy for the design of functionalized devices.[12−18] Most of these structures have been fabricated using hydrothermal reactions, chemical vapor deposition, or ionic-liquid-assisted routes. In the case of hydrothermally grown structures, the morphology can be controlled by moderating the aqueous hydrolysis−condensation growth onto substrates.[19] Also, with application of the hydrothermal strategy, different morphologies of hematite were fabricated besides those mentioned above.[20−29] Solvothermally grown rodlike and flowerlike hematite nanostructures have been used in gas sensors and

Received: September 30, 2010
Revised: March 14, 2011
Published: April 01, 2011

batteries and as photocatalysts.[30,31] Hydrothermal synthesis in a highly basic medium has been used to obtain nanorods,[32] and the solution pH has a profound influence on the morphology.[33]

With the aim of increasing the photocurrent of undoped hematite films, we developed a very simple and effective hydrothermal procedure for modifying the structures of hematite nanoparticles in the pristine film into an array of nanorods, on which flowerlike superstructures evolve upon hydrothermal treatment, as shown in Figure 3. This was achieved by the hydrothermal aftertreatment of the pristine hematite thin film in a closed vessel filled with iron(III) chloride and L-arginine. The amino acid was found to play a decisive role in directing the morphology of the nanostructures. The amino acid assisted hydrothermal method has already been demonstrated for the synthesis of SnO_2 nanocrystals and hematite nanocubes.[34,35] The modified nanostructure grows in a hierarchical fashion from single nanorods to stellate objects. Such sequential growth of the nanostructures follows the same pattern as that observed on WO_3[36] and besides this supports the idea that biomolecules act as effective templates for the growth and self-assembly of nanostructures.[37,38]

EXPERIMENTAL SECTION

Synthesis of a Pristine Hematite Film and Its Corresponding Hydrothermal Treatment. Iron salts, oleic acid, and tetrahydrofuran (THF) used in the synthesis of a hematite film were of reagent grade obtained from Sigma-Aldrich. The amino acid (L-arginine) used was obtained from Sigma-Aldrich, Switzerland (99. 9% pure). Nanostructured hematite (α-Fe_2O_3) thin films were synthesized by the dip coating of a precursor complex on an FTO-coated glass substrate with a withdrawal speed of 1 mm/s, followed by annealing in air at 500 °C for 2 h. The dip coating is a steady process, and here the film thickness is determined by the competition of different forces such as the viscous force, capillary force, and gravity.[39] Faster withdrawal yields generally thicker films. The precursor complex was synthesized by heating a mixture of $Fe(NO_3)_3 \cdot 9H_2O$ (28.0 g) and oleic acid (17.0 g) to 70 °C to give a homogeneous liquid phase.[40] The homogeneous mixture was then heated at 125 °C for 1.5 h to give a reddish-brown viscous mass, which was then cooled to room temperature, left for 24 h, and subsequently treated with 80 mL of THF. The resultant solution was stirred with a glass rod for 30 min and the final powdery precipitate separated from the solution by centrifugation (5000 rpm) for 2−3 min. After centrifugation, the supernatant containing the precursor complex was used for the dip coating of the film. The thicknesses of these pristine hematite films were measured with profilometry and optimized at 600 nm after four-layer deposition.

The flowerlike superstructure along with an array of nanorods was synthesized over the intact hematite film by an amino acid assisted hydrothermal reaction. The pristine hematite film above was first immersed in a solution of $FeCl_3 \cdot 6H_2O$ (5 mmol) and L-arginine (5 mmol) in water (35 mL) in a closed vessel and allowed to react for 48 h at a temperature of 95 °C. After 48 h, the film was removed, washed with distilled water, and dried at room temperature overnight. The dried films were then further characterized by UV−vis spectroscopy, X-ray diffraction (XRD), field-emission scanning electron microscopy (FESEM), transmission electron microscopy (TEM), X-ray photoelectron spectroscopy (XPS), and Brunauer−Emmett−Teller (BET) surface area, and the current density was recorded in a photoelectrochemical workstation.

Characterization. The optical properties of the pristine hematite and hydrothermally modified films were studied by a UV−vis spectrometer (Carry Scan 50). Diffuse-reflectance spectroscopy of pristine and modified films was studied with a Cary 5000(V1.12) UV−vis−near-IR spectrophotometer with an integrating-sphere diffuse-reflectance accessory. The integrating sphere was coated with MgO, and the spectra were referenced against this white material. The film thickness was determined with a stylus profilometer (Ambios XP-100). The phase compositions of the pristine and modified films were examined by powder XRD analysis (PAN analytical X′Pert PRO, Cu Kα radiation). A JEOL JEM 2200 FS transmission electron microscope/STEM operating at 200 keV accelerating voltage was used for TEM analysis. FESEM was performed on a Hitachi S-4800 model. The dark current and photocurrent were recorded with a Voltalab potentiostat in a three-electrode configuration with 1 M KOH (pH = 13. 6) as the electrolyte, Ag/AgCl/saturated KCl as the reference electrode, and a platinum wire as the counter electrode. The Fe_2O_3 film was illuminated on a 0.45 cm^2 area of the electrolyte and a fused silica window with a 0.5 cm^2 circular mask; the total geometric area immersed in the electrolyte was approximately 2.6 cm^2. Sunlight was simulated with a filtered xenon lamp from LOT Oriel. The light intensity was adjusted to AM 1.5 simulated light. XPS spectra were recorded by a PHI LS5600 spectrometer equipped with a Mg Kα X-ray source and calibrated using C1s = 285. 0 eV. The surface areas of the pristine and hydrothermally treated films were obtained by applying the BET technique (Coulter SA3100 series surface area and pore size analyzers) on powders, which were scratched from the films.

RESULTS AND DISCUSSION

Because of the importance of the optical absorption properties and the electronic nature of the band gap in hematite on the solar energy conversion, we have studied changes in the optical properties of hematite with UV−vis spectroscopy after hydrothermal modification. The absorbance spectrum (Figure 1a) shows that hydrothermally modified films absorb at 545 nm, which is the absorption edge of the pristine hematite. Here, the absorption intensity decreases from the pristine film to the 48 h treated film with increasing hydrothermal time. In the case of the sample hydrothermally treated from 2 to 8 h, it remains constant. The 24 h treated sample shows some unusual behavior. It exhibits the same absorption characteristics as those of the pristine film. These variations in the absorption values of pristine and hydrothermally treated films can be explained by considering the effect of the scattering contribution. To obtain quantitative information about the scattering contribution, we applied the Kubelka−Munk (KM) function to the diffuse-reflectance spectra (as shown in the inset of Figure 1d) of the hematite and modified films with the following equation:

$$f(R) = \frac{(1-R)^2}{2R} = \frac{k}{s} \quad (1)$$

R is the diffuse reflectance of the layer relative to a standard such as magnesium oxide, k is the molar absorption coefficient, and s is the scattering coefficient of the sample. The respective diffuse-reflectance spectra can be seen in the inset of Figure 1d. Upon analysis of the reflectance spectra, we found that the scattering coefficient (Figure 1d) varies in a significant manner from the pristine film to the 48 h treated film. The effect is more prominent for 2, 4, and 8 h treated samples between 300 and 600 nm. In the long-term hydrothermally treated samples, the scattering coefficient also changes with the wavelength. The light-scattering properties of the films thus change with the morphology, and the observed optical changes are associated with the changes in the scattering coefficient. This change in the scattering coefficient is basically due to variation in the crystal size and morphology as a result of hydrothermal treatment. In this case, the crystallite size changes as a result of increasing hydrothermal treatment time, as is evident from the crystallite size

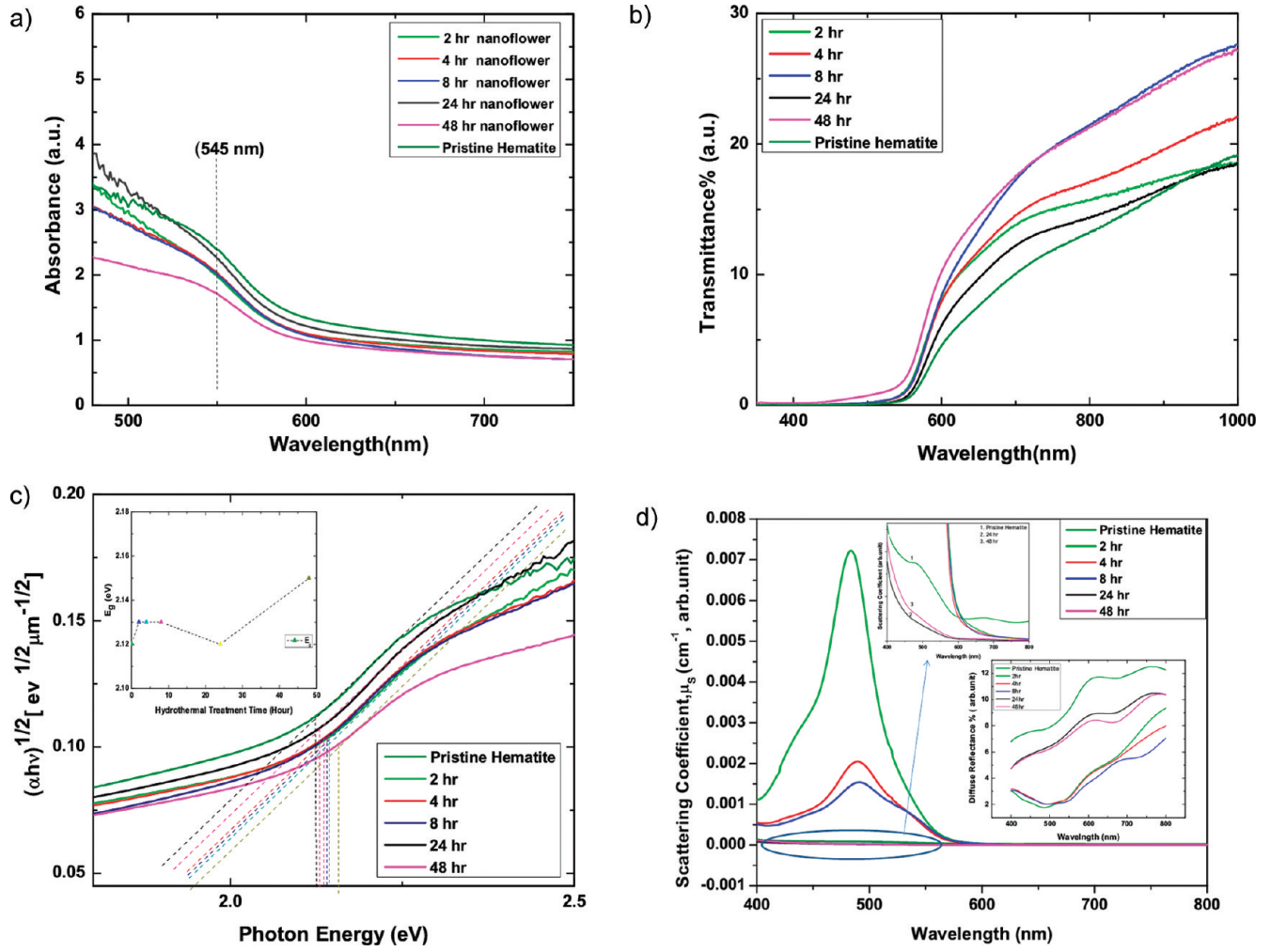

Figure 1. Optical properties of the pristine and modified hematite thin films: (a) absorbance spectra showing the visible-light absorption of hematite at 545 nm; (b) transmittance spectra; (c) evaluation of the optical band gap using the Tauc plot; (d) variation of the scattering coefficient with the hydrothermal time calculated by applying the KM function to diffuse-reflectance spectra (inset).

calculation (Table S1, Supporting Information). It was originally found that variations in the crystal size and morphology[41] altered the scattering and absorption coefficients of goethite and hematite. Another possible reason for the increase in the magnitude of the scattering coefficient is the roughening of the nanoparticle surface after hydrothermal treatment, which affects the mean path length of the rays through the particle, thus decreasing the amount of light absorbed.[42]

From the transmittance spectra (Figure 1b) of the pristine hematite and modified films, we have not found any precise variation in the film transmittance with a corresponding increase in the hydrothermal time, although the transmittance decreases, as is evident by looking at spectra of the modified film with respect to the pristine film in the region λ = 400−800 nm. It is observed that the film becomes more transparent after a 2 h treatment and is enhanced up to 8 h. It becomes again less transparent after 24 h of treatment, which might be due to an increase in the layer thickness from the larger density of a globular flower, as is evident from the FESEM image (Figure 11). Again, at 48 h, the transmittance increases and coincides with the 8 h processed film. These changes in the film transmittance can be explained on the basis of the contribution of different factors. In pristine and hydrothermally treated films, a change in the spectral transmission occurs with an increase in the particle dimensions, which are affected by the interplay of two factors. These are respectively a decrease in the number of scattering centers and an increase in the coefficient of attenuation of light by a single particle.[43] In the region of strong absorption (for hematite, $\lambda \sim$ <600 nm), it was evident from another study that the second factor well prevails over the first one, which leads to a decrease in the spectral transmission with an increase in the particle dimensions. However, in our case, we have not observed a similar trend. It increases with an increase in the dimensions of the particle from the pristine film to the hydrothermally modified film. In the region λ > 600 nm, there is no definite tendency in the variation of the spectral transmission with an increase in the mean particle dimensions. This can also be related to the uncontrolled variations in the structure of the hematite layer with an increase in the mean particle dimensions and morphological change due to hydrothermal treatment. In the next part, we considered the shape of the flower to have some effect on the optical properties. It was already reported that the absorption properties of hematite change as a result of a change in the shape up to 400 nm.[44] To get an idea about the changes that occur, we

dx.doi.org/10.1021/cm102826n |*Chem. Mater.* 2011, 23, 2051–2061

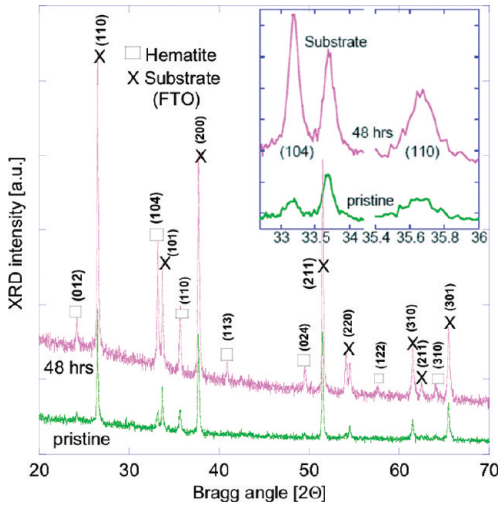

Figure 2. X-ray diffractograms of the pristine and 48 h hydrothermal treatment films.

calculated the band gap of the pristine and modified films using the Tauc plot[45] for indirect transition (Figure 1c), which states that energy bands are parabolic with respect to the crystal momentum. Hematite has an indirect phonon-assisted band-gap transition around 1.9−2.2 eV.[46] The band gap varies slightly with an increase in the hydrothermal treatment time, as is observed from the figure. All of the films show the band gap around 2.12−2.15 eV using a similar Tauc fit and fall within the hematite band-gap range. This pointed out that we have no changes in the electronic structure of the pristine hematite film after hydrothermal treatment. Another interesting observation that can be seen is the change in the slope of the transition with respect to the hydrothermal time and is a maximum in the case of the 48 h treated sample. A similar result was also observed in the case of annealed mesoporous hematite, and this correlated with the nanoparticle size and detailed structural investigation.[47] The slope is proportional to the band tailing parameter (β),[48] which relates the distribution of energy states near the valence and conduction bands. It consistently increases with an increase in the crystalline order and a larger particle size[49] and is validated further from calculation of the nanocrystallite size with an increase in the hydrothermal time, as discussed in the following section.

The X-ray diffractogram of the pristine film shows an overall lower incoherent scattering background than that of the modified film (Figure 2), which signifies that the new flowerlike superstructures and the array of nanorods constitute a larger roughness on the nanoscale than the pristine film. The modified film shows more prominent Bragg reflections than the pristine film. A closer inspection of the diffractograms shows that the intensities of the (104) Bragg reflection in the modified film diffractogram become relatively enhanced when compared with the same reflection in the pristine hematite diffractogram, suggesting an increase of the preferential orientation. This becomes particularly clear when the relative intensities of the (104) reflection are compared with that of the (110) reflection. Initially, in the pristine film, the (104) peak is the same as the (110) peak; see the magnification of the diffractogram in the right part of Figure 2. In the modified film, the (104) peak is larger than the (110) peak. In the pristine film, the (012) and (220) peaks are barely visible, whereas they are well developed in the modified film. The same holds for the (211) and (310) peaks. From the diffractograms of the intermediate modified films (Figure S1, Supporting Information), we observed that the intensities of the (110) and (104) peaks from hematite vary with the treatment time, whereas the substrate peak changes slightly. In the case of the (104) peak intensity, the 2 and 8 h treated films show minimum and maximum values. The intensities of the 18 and 24 h treated films remain almost constant. On the other hand, the (110) peak intensity remains constant for 8, 18, and 24 h treated films and is a minimum for the 2 h treated film. This change in the intensity could be due to a change in the film thickness, as suggested from the optical spectra (Figure 1b). However, a careful comparison of the transmittance spectra with the diffraction data (Figure S1-B, Supporting Information) shows that this is not exactly the case. From here, it can be seen that the 8 h treated film is more transparent than the 24 h film, but its (104) peak intensity reached a maximum in the XRD diffractograms and the (110) peak intensity remained constant, which supports the suggestion of the preferential growth and transformation of a nanoparticle into a nanorod assembly and superstructure. The crystallite size, as determined with the Scherrer equation,[50] increases during hydrothermal processing (Table S1, Supporting Information) along with the primary particle size. From this, we can justify the increase in the band tailing parameter, as is observed in the optical properties of films. In summary, we can say that, while the structural peculiarities of the hematite film, as evidenced by the electron diffraction pattern, are representative only for the modified nanostructures, the X-ray diffractograms provide significant support that the structure of the pristine film undergoes considerable transformation toward the flower-shaped morphology with preferential orientation and a distinct texture difference from those of the pristine hematite, in line with the visual observations on the morphology made by microscopy.

In the morphology study, Figure 3d displays the FESEM micrograph of a typical pristine hematite film with an apparent porosity between the primary particles. The primary particles look like larvae with a smooth surface and have sizes of approximately 50 nm × 100 nm. In the electron micrograph of the film after 48 h of hydrothermal treatment (Figure 3e), we notice several alterations: The smoothness known from the pristine particles has disappeared; the modified particles have a more prismatic geometry. TEM provides further insight into the structure and orientation of the building blocks of the modified hematite film. The particles look more elongated and thinner, like rice grains with a size of around 40 nm × 200 nm, as demonstrated in Figure 4a. The rodlike structures are arranged in a morphology reminiscent of a turflike carpet. Interestingly, superstructures evolve from the nanorods, which look like flowers. A close inspection shows that the superstructures are hexapods with an absolute orthogonality and that their branches are faceted parallel to their long axis (Figure 4b). Employing selected-area electron diffraction along with TEM (Figure 4c) at prominent positions of the hexapods, we found an interesting diffraction pattern that we could crystallographically index with good accuracy. Here, all of the indicated reflections coincide with the ones from the corresponding high-resolution micrographs. The green spots stem from the green rod direction and the red from the other wing. There are quite a few spots not indexed that, nevertheless, show quite some intensity. Because these additional reflections do not correspond to real (possible) hematite crystal spacings, it is likely that they can be attributed to a complex manner of dynamic diffraction within the center of the crossed flower. The lowest-order reflections plus the one along the

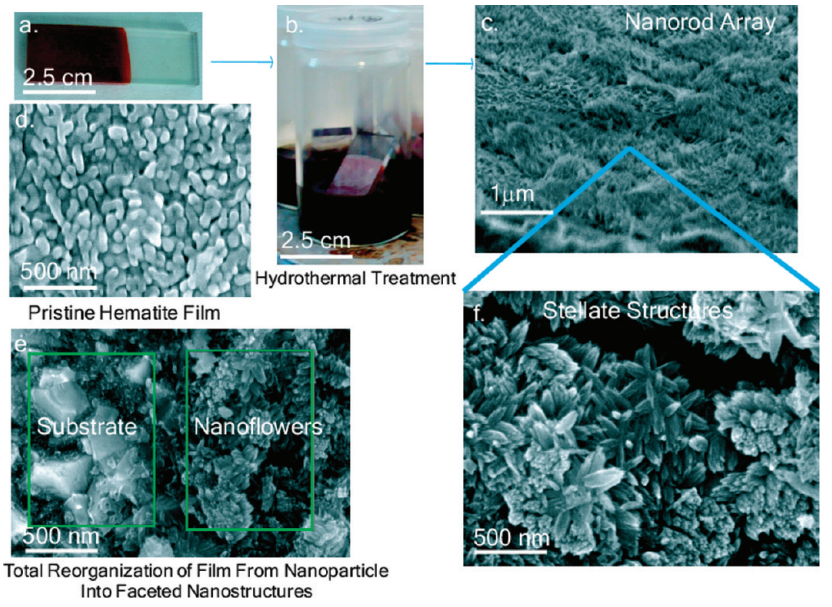

Figure 3. Schemes showing conversion of the pristine hematite film (a) into a film with turflike carpet (c), upon hydrothermal aftertreatment (b), FESEM images of the pristine hematite film (d), and total reorganization of the film (e) into a stellate structure superimposed on the array of nanorods (f).

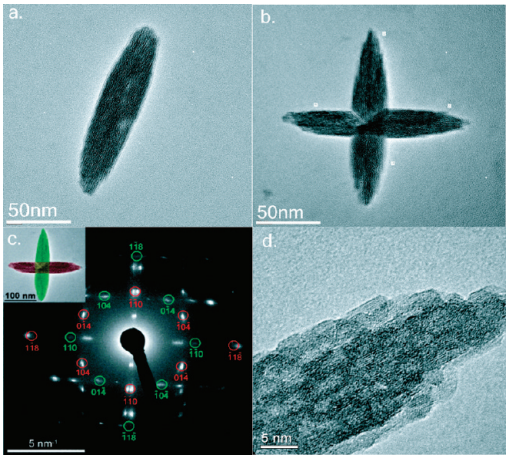

Figure 4. TEM studies of newly formed nanostructures after hydrothermal modification: (a) new hematite particles with rice grain shape; (b) superstructures with an exact orthogonality evolving from the nanorods, which look like flowers; (c) selected-area electron diffraction along with TEM at prominent positions of the multipod structure; (d) higher-magnification image showing that the nanorods have a substructure comprised of subunits of similarly elongated geometry of 2 nm × 5 nm size.

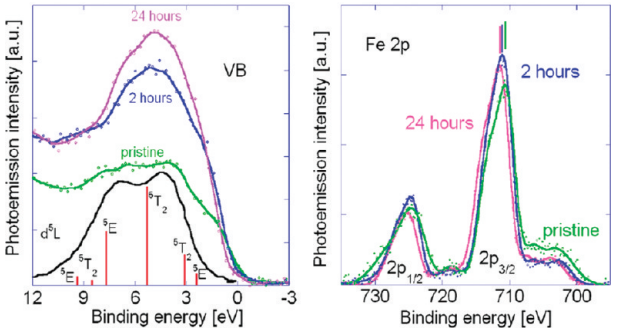

Figure 5. XPS spectra in the valence band (VB) region and Fe 2p core level of pristine and 2 and 24 h hydrothermally treated films. Black VB: theoretical spectrum of hematite.

rod direction were thus only indexed. As pointed out, the rods are inclined, which implies that there can be some intensity mismatch between the different spots compared to a zone-axis-aligned hematite film. Moreover, one also needs to consider that there might be small subgrains, as are observable in the high-resolution TEM micrographs, which are not properly aligned with respect to the main texture. The splitting of the spots along the *y* direction of the diffraction pattern in Figure 4c can be explained by the fact that the horizontal wings are slightly inclined with respect to each other. The incident beam direction is [−221]. It looks like the projection of the rod direction, as seen in the image and the diffraction pattern, is 118, which means that the 110 planes run along the rod direction. The higher-magnification image in Figure 4d shows that the nanorods have a substructure comprised of subunits of similarly elongated geometry of 2 nm × 5 nm size.

The XPS survey scans (Figure S2, Supporting Information) show that the relative carbon concentration on the surface of the films decreases rapidly from 64% to below 35% upon hydrothermal treatment, whereas the relative iron concentration increases from below 6% to above 10% and the chlorine concentration to just below 5%. The valence band range of the XPS spectra (Figure 5) shows a depletion of the spectral intensity near the Fermi energy from the pristine to hydrothermal films. This intensity arises from shoulders at 1.5 eV, which are likely due to a state with e_g orbital symmetry from iron with a $3d^5\underline{L}$ electronic structure in octahedral coordination, compared with the theoretical valence band spectrum of hematite.[51] This structure is diminished upon hydrothermal treatment, when the iron becomes more reduced at the surface, thus probably affecting the photoelectrochemical properties. This is corroborated by a chemical shift of around 1 eV in the Fe 2p core level

dx.doi.org/10.1021/cm102826n |*Chem. Mater.* 2011, 23, 2051–2061

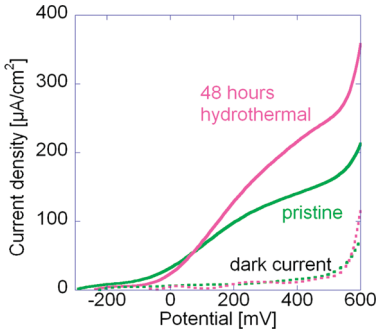

Figure 6. Photocurrent for the pristine and 48 h hydrothermally treated films.

spectra, revealing a partial reduction of the iron at the surface during hydrothermal treatment. An oxygen-depleted surface would fit with the recently proposed suggestion that oxygen chemisorption could play a central role in the photoresponse[52] and the modified films avoid the deleterious effects of grain-boundary recombination.

We measured the photocurrent of the hematite films under AM 1.5 solar light simulation. The pristine film has a saturated photocurrent of 140 μA/cm^2 at 450 mV versus Ag/AgCl scale. Upon hydrothermal treatment, the photocurrent decreases for treatment times of up to 18 h to a value of around 67 μA/cm^2. After further treatment, the photocurrent increases to 157 μA/cm^2 after 24 h and to 218 μA/cm^2 after 48 h. Thus, a 2-day hydrothermal treatment can increase the photocurrent by about 50% (Figure 6). The photocurrent results of the intermediate modified films are shown in Figure S3 (Supporting Information). In all cases, the photocurrent onset is observed at −90 mV and is saturated after 450 mV, followed by the oxidative dark process. The photocurrent generally originates from water oxidation by the photogenerated holes. However, in this case, it might also come from other oxidative processes such as oxidation of residual carbon and Fe $^{2+}$ at the film surface, as suggested by the XPS data. The residual carbons come from the heat treatment of an iron fatty acid complex during synthesis of the pristine hematite film and post hydrothermal modification with L-arginine. So, in order to verify the contributions from carbon and Fe^{2+} oxidation, we performed a cyclic voltammetry (CV) study of the pristine and 48 h treated films under both dark and light conditions at a scan rate of 50 mV/s. From the CV scans of both the pristine and hydrothermally treated films (Figure 7a,b), we did not observe any extra anodic or oxidative peaks in the range of carbon and Fe^{2+} oxidation potentials. Note that the standard electrode oxidation potentials ($E°$) for carbon and Fe^{2+} oxidation are 503 and 770 mV versus a standard hydrogen electrode.[53,54] In our case, the potential of the photoelectrode is reported against a reversible hydrogen electrode (RHE)[7]

$$E_{RHE} = E_{AgCl} + 0.059pH + E°_{AgCl}; \quad E°_{AgCl} = 0.208 \text{ V at } 25 °C \tag{2}$$

by considering the pH of 1 M KOH (~13.83), the electrolyte used during the photoelectrochemical study. Next, during the reverse CV scan, one oxidative peak should come at +0.35 V versus a saturated calomel electrode (or 0.59 V vs Ag/AgCl), which deciphers the removal of the residual carbon species on the hematite surface left due to a processing step.[55] If we express this potential versus Ag/AgCl by applying the above equation, then it

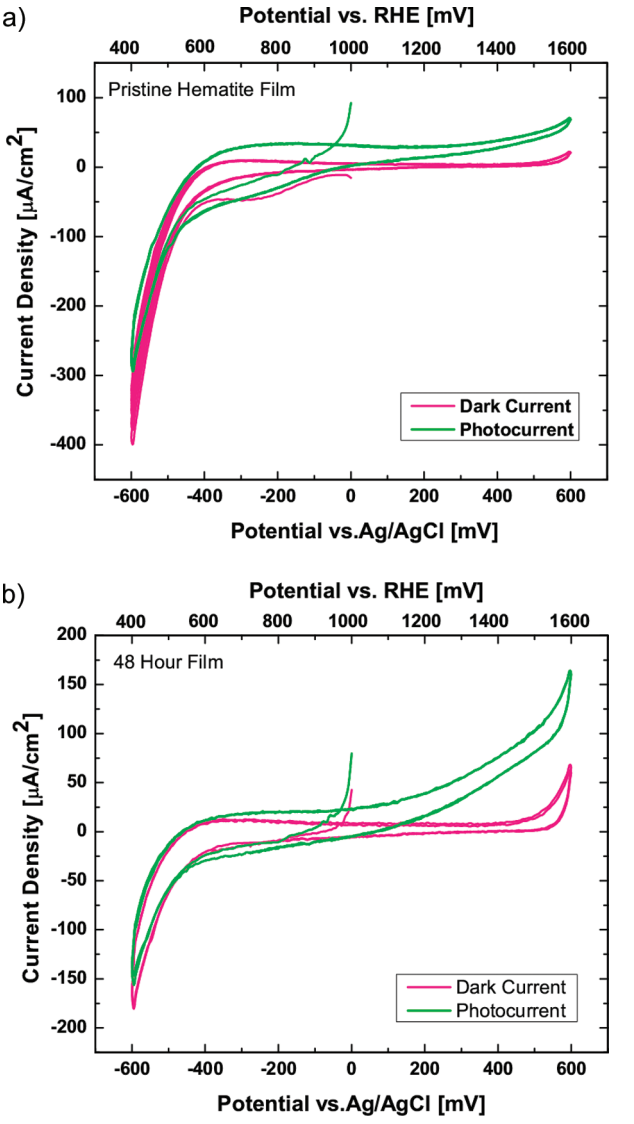

Figure 7. CV results under dark and illuminated conditions: current versus potential of the Ag/AgCl electrode. The scan rate is 50 mV/s, 1 M KOH (pH 13. 8). (a) Pristine hematite film. (b) 48 h hydrothermally processed film.

should be around −434 mV. Also, in another study dealing with the interaction of hydroquinone with the hematite surface,[56] an extra oxidative peak showed the presence of residual carbon, which was not removed during the cleaning process. The cathodic and anodic peaks at the extreme potentials in the CV illustrate decomposition of the solvent such as the reduction and oxidation of water species. In the illuminated condition, the anodic peak increases in both the pristine and hydrothermal conditions. Similarly, in the case of Fe^{2+} oxidation, we also did not observe any extra anodic current near the Fe^{2+} oxidation potential. Following this, we checked the long-term sustainability of the photocurrent by carrying out the chronoamperometric measurement of the hematite film and the 48 h processed film at each of the oxidation potentials of carbon, Fe^{2+}, and water for a suitable period of time. From Figure 8A−D, it is evident that, upon application of the respective carbon and Fe^{2+} oxidation potentials, we did not see any photoanodic current with respect to time in both the pristine and 48 h treated films. Only in the

dx.doi.org/10.1021/cm102826n |*Chem. Mater.* 2011, 23, 2051–2061

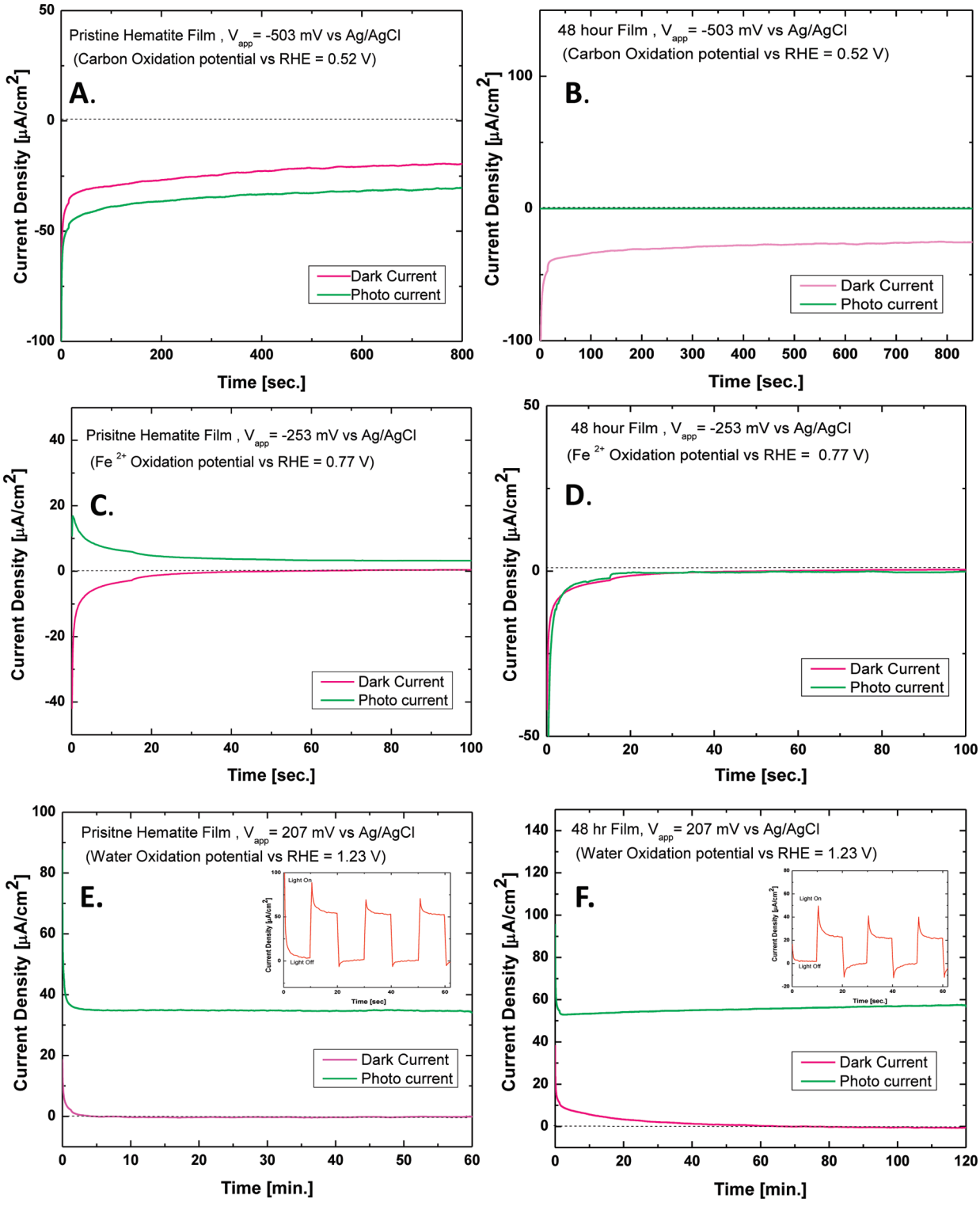

Figure 8. Long-term stability measurement of the photocurrent versus time at −503 mV (A and B), −253 mV (C and D), and 207 mV (E and F) versus the Ag/AgCl electrode for pristine and 48 h processed films. Inset: chopped-light illumination.

case of the pristine film by applying a bias of −253 mV did we observe a small amount of photocurrent, but it is absent in the case of the 48 h treated film. Finally, upon application of the water oxidation potential of 207 mV (1.23 V vs RHE), we found reasonable photocurrent in both the pristine and 48 h treated films, and it is stable up to 1 and 2 h periods of time (Figure 8E,F). In Figure 8F, we observe a small increase in the dark current for the hydrothermally treated film (48 h) at 0.207 V for the first 20 min of chronoamperometric operation. Note, however, that this dark current decays relatively fast over time. To learn about the origin of this dark current, we calculated the total number of moles of electrons generated after 120 min of chronoamperometric operation. This

dx.doi.org/10.1021/cm102826n |*Chem. Mater.* 2011, 23, 2051–2061

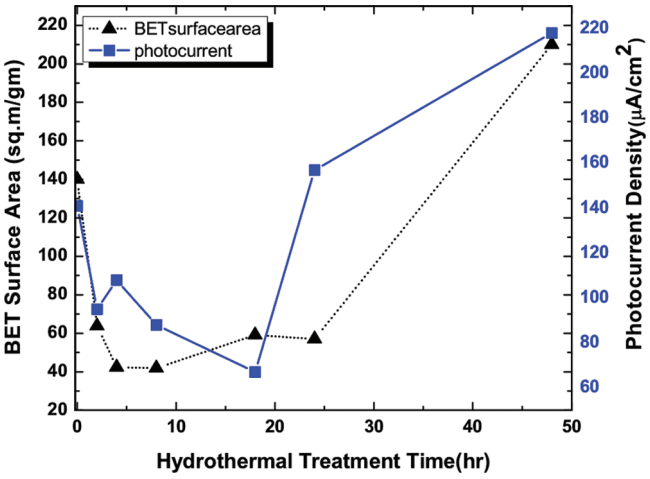

Figure 9. Variation of the BET surface area and photocurrent of modified films obtained at different time evolutions.

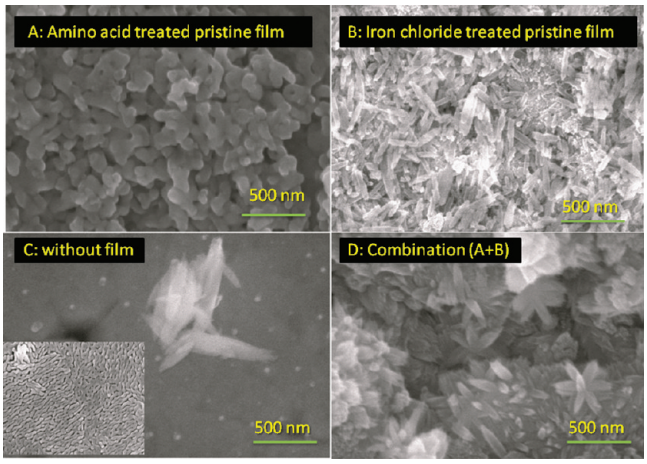

Figure 10. FESEM images: (A) pristine hematite film after treatment with L-arginine (5 mmol); (B) pristine hematite film after treatment with $FeCl_3 \cdot 6H_2O$ (5 mmol); (C) direct hydrothermal synthesis of $FeCl_3 \cdot 6H_2O$ and L-arginine without using the hematite film (5:5 mmol) (inset: hydrothermal treatment of the hematite film with only water); (D) pristine hematite film after treatment with $FeCl_3 \cdot 6H_2O$ and L-arginine (5:5 mmol).

was done by following the procedure described elsewhere (Figure S5, Supporting Information). From this calculation, we find that roughly 102 nmol of electrons gets produced by the oxidation process at the surface of the 48 h modified film. This might arise from the oxidation of Fe^{2+} and residual carbon on the surface of the pristine and modified films, but this oxidation is finished after 20 min. Note that, during recording of the CV, we did not observe any extra current wave due to Fe^{2+} and carbon oxidation because the CV operation was run for a short period. From the preceding discussion, we do accept that the photocurrent is a combination of the oxidation of residual Fe^{2+} and carbon along with water photooxidation. The source of the photocurrent from water oxidation was established by the stability in the photocurrent obtained in both the pristine and hydrothermally modified films (Figure 8E,F). From here, it is also evident that the hydrothermal modification of the original pristine film yields an enhanced photocurrent. Next, in the inset of Figure 8E,F, we demonstrate the chopped-light illumination of both films, where the falling transients (spike) clearly represent photogeneration of an electron acceptor such as a $OH^{\bullet}$ radical. When light is absorbed, electrons are moved from the valence band to the conduction band and the photocurrent is recorded on moving down a potential gradient. The valence band holes move to the surface to oxidize the OH^- ion from electrolyte to make $OH^{\bullet}$.[57,58] The cathodic transient spike arises when $OH^{\bullet}$ at the surface continues to scavenge conduction band electrons due to the light being turned off and $OH^{\bullet}$ being used up. Finally, the oxygen yield has been calculated from the collected charge during chronoamperometric measurement of the hematite and 48 h processed films under dark and light conditions (for the pristine film, 0.12773 C ≡ 1.3237 μmol of electrons, which corresponds to 0.331 μmol of oxygen; for the 48 h treated film, 0.40021 C ≡ 4.1478 μmol of electrons, which corresponds to 1.0369 μmol of oxygen; see Figure S5, Supporting Information).

The next question that naturally arises is, what causes the changes and, in particular, the increase of the photocurrent for the long-time hydrothermally treated films? Potential origins may be of a chemical, morphological, or structural nature. A complementary rationale for the increased photocurrent upon long-term hydrothermal treatment comes from a comparison of the surface areas of the films. To answer this, we carried out BET measurement of the pristine and modified films hydrothermally treated at different time intervals. The BET surface areas for pristine and modified films treated for 48 h are 140 and 210 m^2/g, respectively, which means a 50% increase of the surface area and which quantitatively corresponds to the 50% increase in the photocurrent. Also, from BET analysis of the corresponding intermediate products (Figure 9), we found that the BET surface areas of the films decrease from 2 to 8 h with a consequent increase from 18 to 48 h. Although the 24 h processed film shows almost the same surface area in comparison to that of 18 h, the photocurrent of the 24 h processed film is quite higher. The reasons behind this are still not clear. Afterall, upon a comparison of the BET surface area trend with the corresponding photocurrent data as shown in Figure 9, we found that the photocurrent data vary, to some extent, in a fashion similar to that of the BET surface areas of the modified film. From this study, it is evident that the drop in the photocurrent is due to the reduction of the surface area at middle stages and then an improved surface area at the end of the process. This validated the improved photocurrent performance of the modified film as a result of the effect of increased surface area, measured by BET after a long hydrothermal processing time (48 h).

We further studied the influence of the amino acid in the formation of the flowerlike superstructures and the morphology evolution of the modified films at different times. The hematite nanocrystals that form the modified film are produced through a two-step phase transformation. In the first step, the hematite nanoparticles of the pristine film act as seeds for the formation of nanorods, which form a self-assembled layer having an array of nanorods. In the second step, the nanorods partially transform in a stepwise manner into stellate structures, as shown in Figure 3f. Also, it has been observed that the pristine film morphology completely reorganized into the stellate structure up to the substrate, as is evident in Figure 3e. It is in this process that the amino acid can exert a decisive influence on the size and shape of the hematite nanocrystals.[35] To really understand the role of the presence of both the iron precursor and amino acid, we performed additional control experiments. From the FESEM

dx.doi.org/10.1021/cm102826n |*Chem. Mater.* 2011, 23, 2051–2061

results of the corresponding hematite films treated individually with iron salt, amino acid, and both, we found that only amino acid (L-arginine; Figure 10A) has not transformed the film to a flowerlike form, which renders it ineffective for driving the reaction. Also, upon treatment of the film with $FeCl_3 \cdot 6H_2O$ for 48 h (Figure 10B), we did see some rodlike patterns, but they were just lying on the surface of the pristine hematite film. A blank experiment has also been performed by the hydrothermal treatment of hematite film with water for 48 h at 95 °C (inset in Figure 10C). Here we did not observe any changes in the morphology of the hematite film. Again a direct hydrothermal reaction of $FeCl_3 \cdot 6H_2O$ with L-arginine in the absence of the pristine hematite film (Figure 10C) results in some rodlike structures agglomerated together along with nanoparticles, but no flowerlike morphology was obtained. Finally, upon treatment with both precursors, the original pristine film transformed into faceted structures with the consequent formation of hexapod flowers (Figure 10D). The amino acid L-arginine acts here as a structure-directing agent, and its functional groups $-NH_2$ and $-COOH$ are key components for the controlled crystallization of hematite nanostructures.[59] Biomolecules were recently exploited as structure-directing agents in the synthesis of nanomaterials. For instance, Bi_2S_3 flowerlike patterns with well-aligned nanorods were fabricated using L-cysteine, where the amino acid acts as both a sulfur source and a structure-directing molecule.[60] A peptide such as glutathione was used as the assembling molecule and the sulfur source to synthesize the highly ordered snowflake structure of bismuth sulfide nanorods under microwave radiation.[61] Biostabilized CdS nanoparticles were prepared using cysteine and glutathione, whereby the band-gap energies were adjusted with variation of the pH value, the biomolecules, and the corresponding concentrations.[62] In the next part of the investigation, we studied the time dependence of the morphological evolution of hydrothermally processed films with scanning electron microscopy (Figure 11). From this study, we found that, during the early stages of the hydrothermal reaction, the turflike films of nanorod already started to evolve some globular flowers. These were formed by the hierarchical assembly of individual hematite nanorods mediated by the effect of the amino acid. During the 2−18 h period, these structures were found to be smooth, as observed from the FESEM image, and had less porous character. Upon a further increase in the hydrothermal time, they became more rough and porous until we finally reached 48 h.

Finally, we also illustrated a potential mechanism for the conversion process, as shown in Scheme 1. This is only a possible mechanistic pathway based on the earlier study of the hierarchical assembly of SnO_2 nanorods on hematite nanotubes.[63] The whole process is divided into five stages. The first step involves the formation of $Fe(OH)_3$ by the reaction between $FeCl_3 \cdot 6H_2O$ and L-arginine.[35] The side product of the reaction has also been shown on the top of the arrow. In the next step, heterogeneous nucleation of $Fe(OH)_3$ takes place on the preexisting particle film, which is transformed initially into an akaganeite phase (β-FeOOH)[64] and then oxidized to hematite. Thus, ultimately in step 4, hematite nanoparticles nucleated on the surface of the pristine particles, and this transforms further into a nanorod array by taking a crystallographically preferred direction. Finally, flower-shaped superstructures (stellate object) are formed by the self-assembly processes mediated by the amino acid. This is also supported by the specific role of the amino acid as discussed above. The consequent formation of the hexapod structure after a prolonged hydrothermal time (48 h) could also be triggered by the intrinsic 6-fold symmetry of a hematite crystallite via a combination of the nanorod nucleation

Scheme 1. Illustration of the One-Pot Transformation Process in a Stepwise Manner

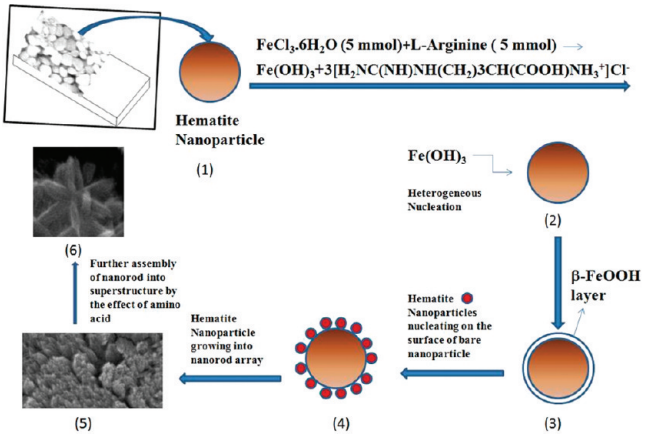

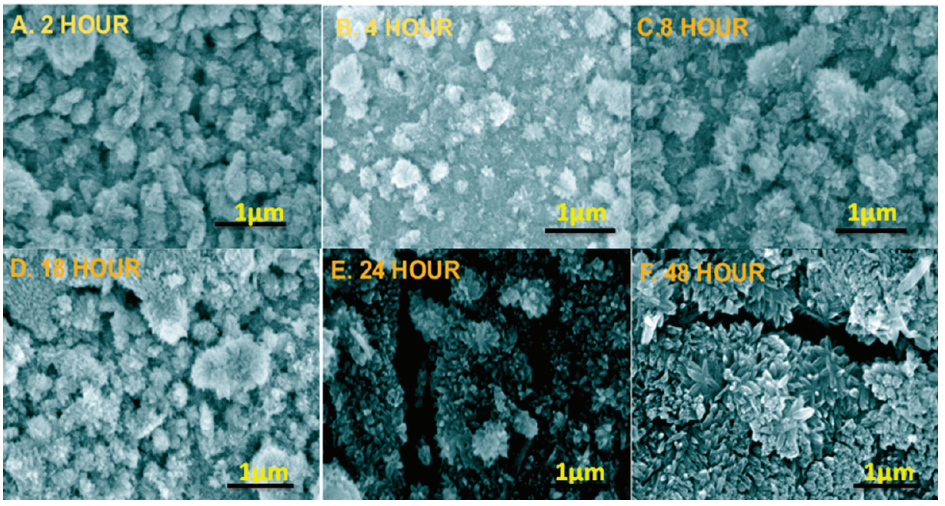

Figure 11. FESEM image of the modified films obtained after (A) 2 h, (B) 4 h, (C) 8 h, (D) 18 h, (E) 24 h, and (F) 48 h of hydrothermal treatment.

dx.doi.org/10.1021/cm102826n |*Chem. Mater.* 2011, 23, 2051–2061

and competing self-assembly process of neighboring parallel nanorods.[36] In another study,[65] it was proposed that when the reaction medium was evaporated to half of its original volume in a period of 16 h, the primary particles self-assembled to form large tetrahedral aggregates. Similar to this observation, we also observed supersaturation of the precursor solution, evident by the solution level reaching two-thirds of its amount after 48 h of hydrothermal treatment. Because of this, structure evolution could not continue and, hence, finally the hexapod structures were reached. The next important observation is the structural evolution of free-standing nanoparticles after hydrothermal treatment for a certain period of time (Figure S4, Supporting Information). This experiment has been done in order to observe the growth of a cluster of nanoparticles into an elongated structure. Normally, the array of nanorods could be easily seen from the FESEM image, but because of their high density, it is difficult to observe the shape evolution of nanoparticles into rods. The details of the formation mechanism will be the subject of the next study. In the current discussion, the unique transformation technique has been described with some potential scenarios.

CONCLUSIONS

In summary, we have developed a simple and effective hydrothermal technique for converting a pristine film of hematite into a film that looks like an array of nanorods with flower-shaped superstructures that showed an enhanced photocurrent. The formation of the superstructure was greatly influenced by the presence of an amino acid. It was found that the 48 h hydrothermally treated film showed a maximum photocurrent with respect to the pristine and intermediate processed films. The hydrothermal treatment further affects the structure, size, and shape of the nanostructure in the modified films, as evidenced by XRD and TEM studies. This influences the optical and surface properties of the modified films. On this basis, it was concluded that the specific morphology along with the higher surface area observed by BET measurement and tuning in the optical response of the modified hematite film favor its higher photoelectrochemical activity. An important advantage of this one-pot conversion method is that the performance of a unique nanostructure in modified films can be directly studied for device-related applications. Also, this technique can be applied to further enhance the efficiency of the hematite film doped with silicon.

ASSOCIATED CONTENT

Supporting Information. XRD patterns of different hydrothermally modified films along with expanded versions of the (104) and (110) peak intensities, XPS survey scans, photocurrent density results of intermediate films, FESEM images, table containing crystallite size calculation, and the procedure for calculating the oxygen concentration from the number of charges collected. This material is available free of charge via the Internet at http://pubs.acs.org.

AUTHOR INFORMATION

Corresponding Author

*Tel: +41(0)58 765 4967. Fax: +41(0)58 7654150. E-mail: debajeet.bora@empa.ch.

ACKNOWLEDGMENT

The research leading to these results received funding from the European Community's Seventh Framework Programme (FP7/2007-2013) Novel Materials for Energy Applications Grant 227179 (NanoPEC, Nanostructured Photoelectrodes for Energy Conversion), the Swiss Federal Office of Energy Contracts 152316-101883, 153613-102809, and 153476-102691, the Indo Swiss Joint Research Programme (ISJRP) Grant JUAF17 (Semiconductor nanowires and nanocomposites for solar cell applications and their photonic characterization), and the Swiss National Science Foundation under Project R′Equip 206021-121306 (Fundamental Aspects of Photocatalysis and Photoelectrochemistry, Basic Research Instrumentation for Functional Characterization).

REFERENCES

(1) Sartoretti, C. J.; Alexander, B. D.; Solarska, R.; Rutkowska, I. A.; Augustynski, J. *J. Phys. Chem. B* **2005**, *109*, 13685–13692.
(2) Watanabe, A.; Kozuka, H. *J. Phys. Chem. B* **2003**, *107*, 12713–12720.
(3) Duret, A.; Gratzel, M. *J. Phys. Chem. B* **2005**, *109*, 17184–17191.
(4) Tahir, A. A.; Upul Wijayantha, K. G.; Saremi-Yarahmadi, S.; Mazhar, M.; Mckee, V. *Chem. Mater.* **2009**, *21*, 3763–3772.
(5) Zhong, D. K.; Sun, J.; Inumaru, H.; Gamelin, D. R. *J. Am. Chem. Soc.* **2009**, *131*, 6086–6087.
(6) Saremi-Yarahmadi, S.; Upul Wijayantha, K. G.; Tahir, A. A.; Vaidhyanathan, B. *J. Phys. Chem. C* **2009**, *113*, 4768–4778.
(7) Kay, A.; Cesar, I.; Gratzel, M. *J. Am. Chem. Soc.* **2006**, *128*, 15714–15721.
(8) Rangaraju, R. R.; Pandey, A.; Raja, K. S.; Misra, M. *J. Phys. D: Appl. Phys.* **2009**, *42*, 135303.
(9) Yang, H. G.; Sun, C. H.; Qiao, S. Z.; Zou, J.; Liu, G.; Smith, S. C.; Cheng, H. M.; Lu, G. Q. *Nature* **2008**, *453*, 638–641.
(10) Warschkow, O.; Ellis, D. E.; Hwang, J.; Mansourian-Hadavi, N.; Mason, T. O. *J. Am. Ceram. Soc.* **2002**, *85*, 213–220.
(11) Sabchez, C.; Sieber, K. D.; Somorjai, G. A. *J. Electroanal. Chem.* **1988**, *252*, 269–270.
(12) An, Z.; Zhang, J.; Pan, S.; Yu, F. *J. Phys. Chem. C* **2009**, *113*, 8092–8096.
(13) Wen, X.; Wang, S.; Ding, Y.; Lin Wang, Z.; Yang, S. *J. Phys. Chem. B* **2005**, *109*, 215–220.
(14) Jia, C.; Sun, L.; Yan, Z.; You, L.; Luo, F.; Han, X.; Pang, Y.; Zhang, Z.; Yan, C. *Angew. Chem., Int. Ed.* **2005**, *44*, 4328–4333.
(15) Chueh, Y. L.; Lai, M. W.; Liang, Q.; Chou, L. J.; Wang, Z. L. *Adv. Funct. Mater.* **2006**, *16*, 2243–2251.
(16) Tang, B.; Wang, G.; Zhou, L.; Ge, J.; Cui, L. *Inorg. Chem.* **2006**, *45*, 5196–5200.
(17) Zhu, L. P.; Xiao, H. M.; Liu, X. M.; Fu, S. Y. *J. Mater. Chem.* **2006**, *16*, 1794–1797.
(18) Cao, M.; Liu, T.; Gao, S.; Sun, G.; Wu, X.; Hu, C.; Wang, Z. L. *Angew. Chem., Int. Ed.* **2005**, *44*, 4197–4201.
(19) Vayssieres, L. *Appl. Phys. A: Mater. Sci. Process.* **2007**, *89*, 1–8.
(20) Katsuki, H.; Komarneni, S. *J. Am. Ceram. Soc.* **2001**, *84*, 2313–2317.
(21) Sun, Q.; Lu, X.; Liang, G. *Mater. Lett.* **2010**, *64*, 2006–2008.
(22) Zhang, X.; Li, Q. *Mater. Lett.* **2008**, *62*, 988–990.
(23) Jing, Z.; Wu, S. *Mater. Lett.* **2004**, *58*, 3637–3640.
(24) Li, W.; Guan, J.; Wang, W.; Tong, G.; Fan, X. *Mater. Chem. Phys.* **2009**, *118*, 496–500.
(25) Liang, M.; Wang, S.; Chang, Y.; Hsiang, H.; Huang, H.; Tsai, M.; Juan, W.; Lu, S. *Ceram. Int.* **2010**, *36*, 1131–1135.
(26) Chen, H.; Zhao, Y.; Yang, M.; He, J.; Chu, P. K.; Zhang, J.; Wu, S. *Anal. Chim. Acta* **2010**, *659*, 266–273.
(27) Wang, W.; Yao, J. *Mater. Res. Bull.* **2010**, *45*, 1672–1678.

(28) Diamandescu, L.; Mihaila-Tarabasanu, D.; Popescu-Pogrion, N.; Totovina, A.; Bibicu, I. *Ceram. Int.* **1999**, *25*, 689–692.
(29) Kandori, K.; Ishikawa, T. *J. Colloid Interface Sci.* **2004**, *272*, 246–248.
(30) Wu, C.; Yin, P.; Zhu, X.; Yang, C. O.; Xie, Y. *J. Phys. Chem. B* **2006**, *110*, 17806–17812.
(31) Zeng, S.; Tang, K.; Li, T.; Liang, Z.; Wang, D.; Wang, Y.; Qi, Y.; Zhou, W. *J. Phys. Chem. C* **2008**, *112*, 4836–4843.
(32) Gou, X.; Wang, G.; Kong, X.; Wexler, D.; Horvat, J.; Yang, J.; Park, J. *Chem.—Eur. J.* **2008**, *14*, 5996–6002.
(33) Vayssieres, L.; Sathe, C.; Butorin, S. M.; Shuh, D. K.; Nordgren, J.; Guo, J. *Adv. Mater.* **2005**, *17*, 2320–2323.
(34) Wu, S.; Cao, H.; Yin, S.; Liu, X.; Zhang, X. *J. Phys. Chem. C* **2009**, *113*, 17893–17898.
(35) Cao, H.; Wang, G.; Warner, J. H.; Watt, A. A. R. *Appl. Phys. Lett.* **2008**, *92*, 013110.
(36) Hu, W.; Zhao, Y.; Liu, Z.; Dunnill, C. W.; Gregory, D. H.; Zhu, Y. *Chem. Mater.* **2008**, *20*, 5657–5665.
(37) Sanchez, C.; Arribart, H.; Giraud Guille, M. M. *Nat. Mater.* **2005**, *4*, 277–288.
(38) Sarikaya, M.; Tamerler, C.; Jen, A. K. Y.; Schulten, K.; Baneyx, F. *Nat. Mater.* **2003**, *2*, 577–585.
(39) Scriven, L. E. *Mater. Res. Soc. Symp. Proc.* **1988**, *121*, 717–729.
(40) Deb, P.; Basumallick, A.; Sen, D.; Mazumder, S.; Nath, B. K.; Das, D. *Philos. Mag. Lett.* **2006**, *86*, 491.
(41) Cornell, R. M.; Schwertmann, U. *The Iron Oxides—Structure, Properties, Reactions, Occurrence and Uses*; VCH Verlagsgesellschaft mbH: Weinheim, Germany, 1996.
(42) Bruce, H. *Theory of Reflectance and Emittance Spectroscopy*; Cambridge University Press: Cambridge, U.K., 1993.
(43) Baikov, M. V.; Ponyavina, A. N.; Prishivalko, A. P.; Sviridov, V. V.; Sil'vanovich, N. I. *J. Appl. Spectrosc.* **1996**, *63*, 297–303.
(44) Wang, J.; White, W. B.; Adair, J. H. *J. Am. Ceram. Soc.* **2005**, *88*, 3449.
(45) Tauc, J.; Grigorov, R.; Vancu, A. *Phys. Status Solidi* **1966**, *15*, 627.
(46) Kennedy, J. H.; Frese, K. W. *J. Electrochem. Soc.* **1978**, *125*, 709.
(47) Sivula, K.; Zboril, R.; Formal, F. L.; Robert, R.; Weidenkaff, A.; Tucek, J.; Frydrych, J.; Gratzel, M. *J. Am. Chem. Soc.* **2010**, *132*, 7436–7444.
(48) Sharma, P.; Vashistha, M.; Jain, I. P. *J. Optoelectron. Adv. Mater.* **2005**, *7*, 2647.
(49) Iribarren, A.; Castro-Rodrigruez, R.; Sosa, V.; Pena, J. L. *Phys. Rev. B* **1998**, *58*, 1907.
(50) Patterson, A. L. *Phys. Rev.* **1939**, *56*, 978–982.
(51) Fujimori, A.; Saeki, M.; Kimizuka, N.; Taniguchi, M.; Suga, S. *Phys. Rev. B* **1986**, *34*, 7318.
(52) Yu, X.; Cao, C. *Cryst. Growth Des.* **2008**, *8*, 3951–3955.
(53) www.electrochem.org/meetings/scheduler/abstracts/214/0989.pdf.
(54) www.siliconfareast.com/ox_potential.htm.
(55) Jingyu, S.; Jianshu, H.; Yanxia, C.; Xiaogang, Z. *Int. J. Electrochem. Sci.* **2007**, *2*, 64–71.
(56) Stack, A. G.; Eggleston, C. M.; Engelhard, M. H. *J. Colloid Interface Sci.* **2004**, *274*, 433–441.
(57) Eggleston, C. M.; Shankle, A. J. A.; Moyer, A. J.; Cesar, I.; Grätzel, M. *Aquat. Sci.* **2009**, *71*, 151–159.
(58) Brimblecombe, R.; Koo, A.; Dismukes, G. C.; Swiegers, G. F.; Spiccia, L. *J. Am. Chem. Soc.* **2010**, *132*, 2892–2894.
(59) Orme, C. A.; Noy, A.; Wierzbieki, A.; McBride, M. T.; Grantham, M.; Teng, H. H.; Dove, P. M.; DeYoreo, J. J. *Nature* **2001**, *411*, 775.
(60) Zhang, B.; Ye, X.; Hou, W.; Zhao, Y.; Xie, Y. *J. Phys. Chem. B* **2006**, *110*, 8978–8985.
(61) Lu, Q.; Gao, F.; Komarneni, S. *J. Am. Chem. Soc.* **2004**, *126*, 54.
(62) Barglik-chory, Ch.; Remenyi, Ch.; Strohm, H.; Müller, G. *J. Phys. Chem. B* **2004**, *108*, 7637.
(63) Zhang, D.; Sun, L.; Jia, C.; Yan, Z.; You, L.; Yan., C. *J. Am. Chem. Soc.* **2005**, *127*, 13492–13493.
(64) Nakamura, T.; Kurokawa., H. *J. Mater. Sci.* **1995**, *30*, 471.
(65) Wang, W.; Howe, J. Y.; Gu, B. *J. Phys. Chem. C* **2008**, *112*, 9203–9208.